Surfaces and Interfaces 17 (2019) 100347

Contents lists available at ScienceDirect

Surfaces and Interfaces

journal homepage: www.elsevier.com/locate/surfin

Opto-electronic properties of anodized TiO_2 nanotube arrays investigated using electron energy loss spectroscopy

Franscious Cummings[a,*], Anele Tshaka[b]

[a] Electron Microscope Unit, University of the Western Cape, Private Bag X17, Bellville 7535, South Africa
[b] Department of Physics and Astronomy, University of the Western Cape, Private Bag X17, Bellville 7535, South Africa

ARTICLE INFO

Keywords:
Anodization
TiO_2 nanotubes
Electron energy loss spectroscopy

ABSTRACT

A study of the nanoscale crystallinity of anodized TiO_2 nanotubes is reported with the aim of demonstrating its influence on the localized optical and electronic properties of the structure. By employing scanning transmission electron microscopy, coupled with electron energy loss spectroscopy, x-ray diffraction and electron energy filtered jump-ratio imaging to probe changes in the electron near edge fine structure of the Ti $L_{3,2}$ ionization edge, it is found that nanotubes annealed at 450 °C in air for 3 h crystallize in the anatase polymorph along their walls, with the underlying thick oxide barrier layer being predominantly rutile. An increase in annealing temperature to 600 °C results in the co-existence of anatase and rutile along the nanotube length with the nanotube top and bottom showing crystallization in anatase and rutile, respectively. Valence EELS shows that the localized energy band-gap is inconsistent along the nanotube length, deviating between that typically measured for anatase (3.2 eV) and rutile (3.0 eV). The obtained band-gap of 3.21 eV at the nanotube top and 3.44 eV at nanotube bottom is attributed to the co-existence of anatase and rutile phases even at a low annealing temperature of 450 °C.

1. Introduction

A broad range of applications incorporate one-dimensional (1D) nanostructured forms of TiO_2 containing both rutile and anatase crystalline phases [1–4]. Of particular interest is highly ordered anodized TiO_2 nanotubes (ATNTs) [5,6], which have been vigorously studied for their high surface area and one-dimensional nature that act as efficient charge collectors with 1D pathways in applications for renewable energy sources [7–8], energy scavenging [9] and energy storage as batteries [10]. Although the formation mechanism during the anodization process is well documented, as schematically depicted in Fig. 1(a) and (b), a holistic description of the crystallinity throughout the nanotubular structure is non-evident, even though it has been shown to exist as a hybrid anatase/rutile structure upon annealing [11–13]. Scanning transmission electron microscopy coupled electron energy loss spectroscopy (STEM-EELS) provides a fundamental means of detecting and quantifying the valence states in transition metal-oxides [14–16], as well as the localized electronic structure-related optical behavior, or the so-called opto-electronic properties, such as the bandgap [17,18]. In addition, modern STEM-EELS set-ups in aberration corrected transmission electron microscopes are now capable of collecting elemental maps with atomic resolution [19–21], as well as detecting individual atoms in materials and producing elemental maps of impurities in low concentrations [22–26]. Each polymorph of a particular crystal exhibits a unique EELS profile, thereby allowing the technique to be suitably used as a profiling mechanism to identify each structure on the submicron to nanoscale. In turn, by knowing these fundamental properties on these scales, a clear deduction of how they influence the bulk crystallinity, for example, can be elucidated. In a typical EELS spectrum the local environment of the metallic and oxygen atoms is characterized by a fine structure of the onset of the respective ionization edges. This is known as electron energy-loss near edge fine structure (ELNEFS). During ELNEFS analyses the $L_{3,2}$ line-shapes of the 3d transition metals contain information about the valence state, as well as the coordination and site symmetry of the central atom [14,15]. The L_3 edge originates as a result of electron transitions from the inner $2p_{3/2}$ orbitals to empty 3d orbitals in the metal, whereas the L_2 edge originates from $2p_{1/2} \rightarrow 3d$ electron transitions. In the case of TiO_2 the fine-structure of the $L_{3,2}$ edges mainly reflect the covalent bonding states resulting from direct and/or indirect interactions between O and Ti atoms. To understand the ELNEFS signals of either rutile or anatase, a detailed discussion of the respective space groups is required. Both systems are tetragonal with rutile containing six atoms per unit cell, anatase twelve and the Ti atom being coordinated to six oxygen atoms; in turn, each oxygen atom is

* Corresponding author.
E-mail address: fcummings@uwc.ac.za (F. Cummings).

https://doi.org/10.1016/j.surfin.2019.100347
Received 10 May 2019; Received in revised form 18 June 2019; Accepted 22 June 2019
Available online 23 June 2019

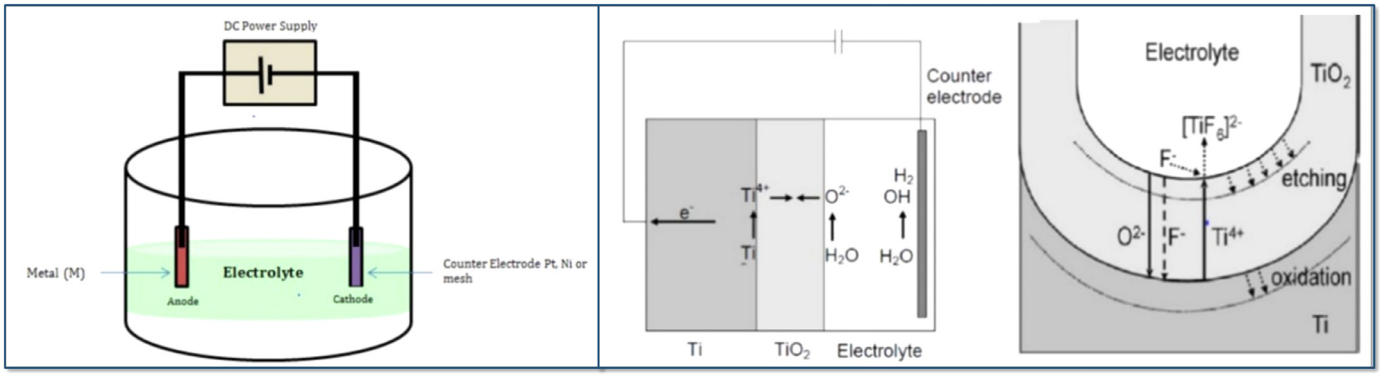

Fig. 1. Experimental set-up used in this work to synthesize ATNTs and the growth model as discussed in [4].

coordinated to three Ti atoms. The oxygen octahedron around the titanium atom is slightly distorted and in both cases two Ti-O distances are slightly greater than the other four. This is accompanied by either some or all of the O-Ti-O bond angles deviating from 90°, which lowers the local point-group symmetry around the Ti atom from O_h to D_{2h} in rutile and Oh to D_{2d} in anatase. Rutile and anatase differ in structure by the secondary coordination of the TiO_6 octahedra: in rutile two edges are shared and in anatase four. The two lowest unoccupied molecular orbitals of rutile are mostly Ti 3d and O 2p in nature, which separate into a threefold t_{2g} and twofold e_g orbitals known as the crystal field orbitals. In perfect O_h symmetry (i.e. in the absence of the TiO_6 octahedron distortion), these two orbitals will be manifested in two distinct levels, i.e. L_2 and L_3 with their maxima separated by 4.5 eV. However, the D_{2h} symmetry of rutile results in the splitting of t_{2g} into b_{3g}, a_g and b_{2g} sub-orbitals, whereas the e_g band split into b_{1g}, and a_g levels. Similarly, the L_2 and L_3 ionization edges of anatase also split into threefold t_{2g} and two fold e_g suborbitals [27–30]. Example spectra of these ionization edges will be presented elsewhere in this manuscript.

Stayanov et al. [31] used ELNEFS measurements in combination with density functional theory calculations to quantify the valence state, local site coordination, as well as the concentration of crystalline versus amorphous phases present in powdered forms of Ti_xO_y polymorphs. It was shown that the effects of polyhedra distortions for oxides with mixed Ti^{3+}/Ti^{4+} valence states, i.e. Ti_4O_7 and Ti_5O_9, result in a prominent pre-peak in the Ti L_3 edge. In addition, a systematic chemical shift of the Ti white lines of up to 2 eV per valence state was noticed, with the ELNEFS signal of the corresponding oxygen K edge being sensitive to covalent bonding in all the analyzed oxides. Bertoni et al. [32] used EELS to quantify the amorphous and crystalline phases of mesoporous TiO_2 by fitting a superposition of core-loss edges using a maximum likelihood method with measured reference spectra. The study showed that the absolute amount of crystalline phases in the specimen can be determined to an accuracy below 5%, with the technique also allowing for the quantification of the amorphous content in the structure, unlike X-ray powder diffraction. ATNTs offer a complex, yet interesting network of intercalated nano-crystals of Ti_xO_y, compacted in tube form, separated by weakly interacting Van der Waals forces [33]. As is the case for most nanocrystals, this intertwined network of crystallites, predominantly anatase and rutile in nature, offer intricate localized properties, often causing uncertainty around their effect on the measured bulk properties. In particular, a clear understanding of how the inhomogeneous ATNT crystallinity affects the localized opto-electronic properties, which are crucial to quantify before application in the broad spectrum of devices often reported, remains largely unexplored. On the few publications exploring this broad topic, Akita et al. [34] showed by means of EELS that the crystalline structure of hydrothermally synthesized nanotubes differed subtly to that of the bulk anatase and/or rutile TiO_2 structure. Regonini et al. [35] deconvoluted Ti $L_{3,2}$ ionization edges of ATNTs fabricated with varying water concentrations, to show that both Ti^{2+} and Ti^{3+} states are present in the sample in addition to the Ti^{4+} valence of rutile and anatase. From these studies it is evident that more insights are required to interpret the ELNEFS of TiO_2 nanotubes. As such, in this contribution STEM-EELS coupled with energy filtered transmission electron microscopy (EFTEM) imaging and elemental analyses form the core investigative tools to probe the nano-scale properties of TiO_2 nanotube arrays. Three different regimes of electrolyte solutions are used for nanotube synthesis during the study, which allows for different nanotube growth rates, ultimately yielding different morphological structures. These differences in nanotube structure, in turn, offer distinct architectures for crystal formation upon subsequent annealing of the nanotubes at either 450 or 600 °C in air at atmospheric pressure.

2. Material and methods

2.1. Synthesis of one-dimensional TiO_2 nanotube arrays in different electrolyte compositions

An acidic, aqueous based electrolyte solution (electrolyte 1, pH = 2.61) was prepared by dissolving 0.14 mol/l of sodium fluoride (NaF) salt in 97 vol% deionized water followed by room temperature magnetic stirring for 5 min. During the stirring process, 0.5 mol/l of phosphoric acid (H_3PO_4) was added to the solution. A second electrolyte (electrolyte 2, pH = 7.47) consisted of 1.0 mol/l of NaF dissolved in 2 vol% deionized water and 97 vol% of glycerol. The solution was rigorously stirred 60 °C for 20 min and allowed to cool to room temperature prior to anodization. The final electrolyte (electrolyte 3, pH = 7.67) was prepared by dissolving 0.14 mol/l of ammonium fluoride (NH_4F) in 2 vol% deionized H_2O before adding 97 vol% of polyethylene glycol (PEG). The solution was once more stirred at 60 °C for 20 min and allowed to cool to room temperature before use. All chemicals used were of chemical grade, obtained from Sigma-Aldrich (Pty) Ltd, South Africa.

The TiO_2 nanotube arrays were grown by immersing 50 μm thick titanium foil (Ti, 99.99% purity, Goodfellow, United Kingdom) in the three different electrolyte regimes at various anodization potentials and time. Prior to synthesis, the Ti foils were sectioned into 1 × 1.5 cm^2 rectangles, washed in a successive baths of methanol, ethanol and isopropanol under ultrasonic bath agitation, followed by drying in a dry nitrogen stream. A platinum mesh, of 1 × 1.5 cm^2 dimension, was used as the counter electrode for all experiments. For each electrolyte system a parametric study was performed to obtain the optimized growth conditions, yielding repeatable nanotube morphologies; Table 1 summarizes these conditions for each system. All nanotubes were annealed at 450 and 600 °C for 3 h in air at atmospheric pressure, post anodization.

Table 1
Optimized conditions for repeatable synthesis of TiO_2 NWs in different electrolyte regimes.

	pH	Electrolyte composition	Voltage (V)	Time (h)
Electrolyte 1	2.61	0.14 mol/l NaF + 0.5 mol/l H_3PO_4 + 97 vol% H_2O	30	3
Electrolyte 2	7.47	1.0 mol/l NaF + 2 vol% H_2O + 97 vol% glycerol	60	4
Electrolyte 3	7.67	0.14 mol/l NH_4F + 2 vol% H_2O + 97 vol% PEG	60	24

2.2. Sample characterization

The morphology of the nanotubes was studied with a Zeiss Auriga field emission gun scanning electron microscope (FEG-SEM), operated at 5 kV and employing an in-lens secondary electron detector at working distances below 5 mm for high resolution imaging. The crystallinity of the nanotubes was studied with x-ray diffraction (XRD), recorded with a PANalytical X'Pert Pro diffractometer, operated at 45 kV and 40 mA at the source. Copper $K_{\alpha 1}$ radiation with a wavelength of 0.154 nm was used as the x-ray source. The atomic structure was studied with an FEI Tecnai F30 field-emission gun transmission electron microscope (FEG-TEM) operated at 300 kV and equipped with a Fischione high angular annular dark field (HAADF) detector for high Z-contrast imaging in STEM mode using an electron probe size between 0.1 and 0.2 nm. A Gatan Image Filter (GIF-Tridiem) was used to record the electron energy loss spectra in STEM mode at an energy resolution and dispersion of 0.8 eV and 0.2 eV/channel, respectively. A STEM convergence angle of 3.33 mrad and collection angle of 8.87 mrad were used for all experiments.

3. Results and discussion

Fig. 2 compares top- and side-view SEM micrographs of the ATNTs synthesized using the three electrolyte systems listed in Table 1. From the top-view images the average nanotube diameter and wall-thicknesses were determined, whereas the cross-sectional images allowed for measurement of the nanotube lengths; the results are listed in Table 2. As shown, anodization in type 2 and 3 electrolytes, for longer periods yields nanotubes with high aspect ratios compared to those obtained when using acidic electrolyte 1 at shorter synthesis times. Synthesis in these electrolytes at the same anodization time and voltage as the regime 3 electrolyte yielded inconsistent growth. This is ascribed to the slow, constant growth rate of nanotubes as a result of the low diffusion rate of fluoride ions in the highly viscous PEG and glycerol electrolytes. The longer synthesis periods also allow for the formation thicker oxide layers, which is in turn continuously etched into a pit network and ultimately into longer nanotubes [8]. In contrast, even though it is known that organic electrolytes with reduced water concentrations below 5 vol% yield nanotubes of lengths exceeding 10 μm, the nanotubes synthesized in electrolyte 2 yielded the shortest lengths of the organic electrolytes employed. This is attributed to a lower donation of

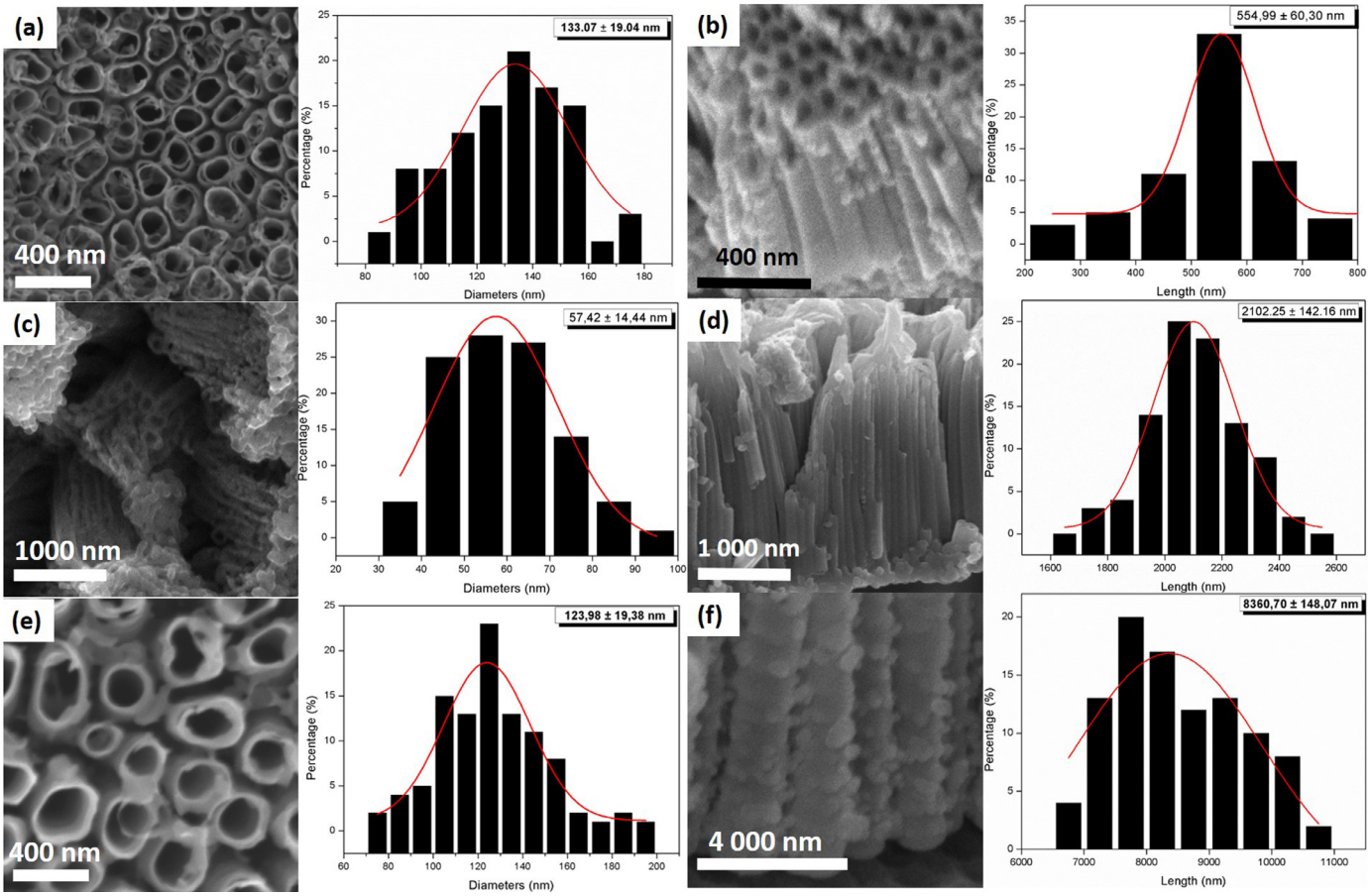

Fig. 2. Top and cross-sectional SEM micrographs with histograms of the diameter and nanotube length: (a)-(b) regime 1, (c)-(d) regime 2 and (e)-(f) regime 3 electrolytes.

Table 2
Morphological and structural properties of the ATNTs synthesized in different electrolytes.

Parameter	Electrolyte 1	Electrolyte 2	Electrolyte 3
Diameter (nm)	133.77 ± 19.04	57.42 ± 14.44	123.98 ± 19.38
Wall thickness (nm)	20.20 ± 5.18	27.83 ± 1.72	18.25 ± 1.84
Length (nm)	554.99 ± 60.30	2102.25 ± 142.16	8360.70 ± 148.07
Aspect ratio	4.15	36.61	67.44
Annealed at 450 °C			
Anatase a, c (nm)	0.387; 0.849	0.382; 0.911	0.378; 0.958
Anatase cell volume (x 10^{-3} nm^3)	127.15	132.94	136.88
a/c ratio	0.456	0.419	0.395
Anatase crystallite size (nm)	40.39 ± 1.01 nm	58.06 ± 1.45 nm	58.08 ± 3.45 nm
Rutile a, c (nm)	0.459; 0.300	0.456; 0.304	0.460; 0.300
Rutile cell volume (x 10^{-3} nm^3)	63.20	62.21	63.48
a/c ratio	1.530	1.500	1.533
Rutile crystallite size (nm)	11.96 ± 0.30 nm	10.08 ± 0.25 nm	10.07 ± 0.1 nm
Rutile/anatase relative%	21.26/78.74	3.42/96.58	8.35/91.65
Annealed at 600 °C			
Anatase a c (nm)	0.378; 0.926	0.378; 0.931	0.378; 0.942
Anatase cell volume (x 10^{-3} nm^3)	132.31	133.03	134.60
a/c ratio,	0.408	0.406	0.401
Anatase crystallite size (nm)	58.08 ± 1.45 nm	47.43 ± 1.19 nm	47.41 ± 1.19 nm
Rutile a, c (nm)	0.457; 0.297	0.457; 0.297	0.459; 0.296
Rutile cell volume (x 10^{-3} nm^3)	62.03	62.03	62.36
a/c ratio	1.539	1.539	1.551
Rutile crystallite size (nm)	73.87 ± 1.85 nm	73.85 ± 0.25 nm	56.74 ± 1.42 nm
Rutile/anatase relative%	57.92/42.08	65.63/34.37	51.41/48.59

O^{2-} species from the glycerol rich electrolyte, subsequently resulting in thinner oxide layer formation and hence faster barrier breakdown, thereby leading to termination of the nanotube growth [36]. A further contributing factor is the incorporation of organic components from the electrolyte into the oxide film, which reduces the permittivity of the oxide layer and increases its dielectric breakdown potential [37].

The use of a high anodization potential and fluoride concentration in type 2 electrolytes, greatly enhance breakdown of the formed oxide layer, in an attempt to minimize the foreign ion incorporation, and could explain the resultant narrower diameters shown in Fig. 2. At closer inspection it is also apparent that TiO_2 nanotubes synthesized in the glycerol based electrolyte have smoother side-walls compared to those obtained from type 1 and 3. This is attributed to local acidification [11,13] at the tube bottom that increases the dissolution rate of the formed compact layer. A further interesting feature is the bunching/branching of the nanotubes when synthesized in glycerol based electrolytes. Branching of TiO_2 nanotubes during anodization in glycerol electrolytes has been reported by Anitha et al. [38] who employed a two-step potentiostatic anodization method and ascribed the occurrence to the different ramping rates used during synthesis. One possible explanation for the observed structures of Fig. 2(c) and (d) may lie in the smaller nanotube pore diameter and wall thicknesses, shown in Table 2. The smaller pores are directly linked to the pit sizes, as discussed above, which in turn, are driven by the diffusion coefficient of the electrolyte system used. In this case, when using the glycerol system, a much higher areal density of nanotubes is obtained, as shown by Fig. 2(c), which subsequently yield the bunched ropes of nanotubes. As a result of this high density and the continuous etching of the oxide layer, the available space for continuous oxide formation becomes limited and since saturation is not yet attained, alternative pathways of etching are found, subsequently leading to the branched nanotube structures.

The XRD patterns of Fig. 3(a) show that annealing at 450 °C in air for 3 h leads to crystallization of the NTs into anatase TiO_2 (JCPDS 00–001–0562), with preferred growth direction along ⟨101⟩. Low intensity diffraction of rutile TiO_2 (JCPDS #00–001–1292) are also noticed, emanating from the (110), (101) and (211) planes at 2θ = 27.50, 36.14 and 54.21°, respectively. In contrast, annealing at 600 °C sees the rutile phase becoming more prominent with a preferred orientation along ⟨110⟩ at 2θ = 27.50° noted for all three regimes of synthesis. The anatase unit cell is of the $I4_1/amd$ spacegroup with theoretical unit cell dimensions $a = b = 0.373$ nm, $c = 0.937$ nm and unit cell volume = 130.36×10^{-3} nm^3, whereas rutile has a $P4_2/mnm$ spacegroup with unit cell dimensions of $a = b = 0.458$ nm, $c = 0.295$ nm and unit cell volume = 61.88×10^{-3} nm^3. The relative percentage of rutile to anatase is shown in Table 2; this was determined by comparing the relative integrated area under the rutile (110) peak to the total integrated area of the rutile (110) and anatase (101) diffraction peaks. Peaks from the remnant titanium foil used during anodization are also observed and labeled accordingly in Fig. 3. A study of the anatase and rutile unit cell parameters, as listed in Table 2, shows a linear increase in the anatase unit cell volume, mainly caused by an increase in the length of c; the a/c ratio decreases from 0.456 for electrolyte 1 to 0.395 for NTs synthesized in electrolyte 3. The rutile cell parameters show no obvious change in size or unit cell parameters for any of the three different synthesis conditions, when annealed at 450 °C. This is attributed to the low rutile content in the sample, with very small crystallite size as shown in Table 2, packed in-between the prevailing anatase network of large crystallite size (> 40 nm in diameter). The crystallite sizes are calculated using the modified Williamson-Hall method reported by Mote et al. [39]. At further inspection it is also found that the anatase size linearly increases with aspect ratio, whereas insignificant change in rutile size is noted. This is attributed to the fact that during initial crystal formation, the small rutile crystallites form the seed layer for anatase structure formation [40,41], with the larger anatase unit cells subsequently packing in the tetragonal packing arrangement, which may be considered as a special distorted hexagonal close pack arrangement, to form the side walls of the nanotubes. These attributes also can be used to explain the differences in anatase-to-rutile crystalline volume fractions determined and listed in Table 2. Of course, the rate of oxide breakdown and subsequent nanotube growth termination, as controlled by the different diffusion rates in the various electrolytes as well as anodization voltage employed, once more determine the size of wall thickness as tabulated in Table 2.

As shown, at 600 °C the rutile content markedly increases, but as the case when annealed at 450 °C, no obvious change in unit cell parameters or volume are detected. In contrast, the anatase crystal structure now also shows negligible change in parameter or volume of the unit cell for the three respective electrolyte synthesis conditions. As shown at the bottom of Table 2, the average rutile crystallite sizes are almost

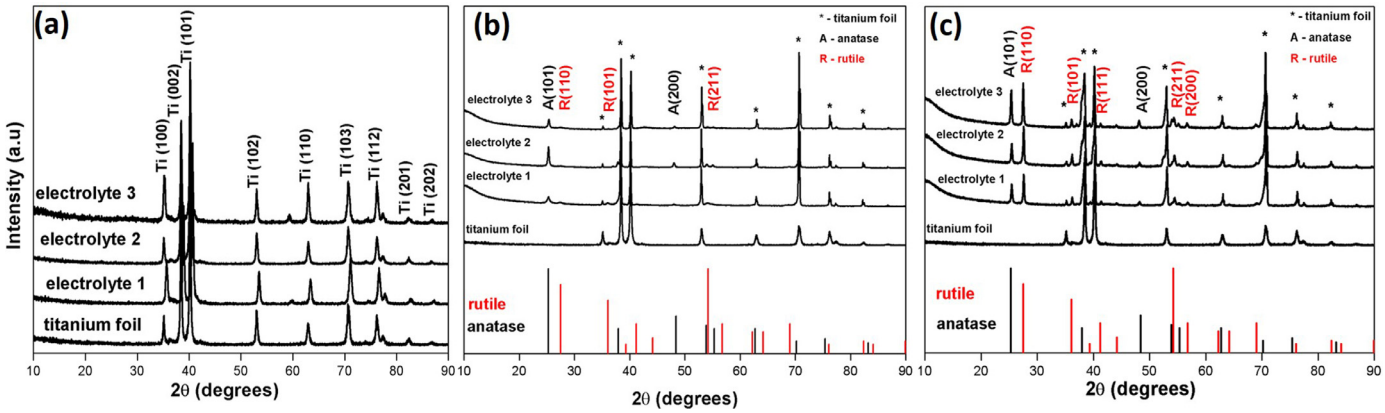

Fig. 3. XRD patterns of the ATNTs (a) as-synthesized; (a) annealed at 450 and (b) 600 °C for 3 h in air at atmospheric pressure.

seven times greater upon annealing at 600 °C compared to 450 °C, whereas the anatase sizes remain largely unchanged. This suggests that an annealing temperature of 600 °C allows for a full evolution of the crystal growth of the nanotubes into a stable rutile/anatase hybrid phase. The transformation of anatase to rutile is explained by Varghese et al. [41], who ascribed the phenomenon at high annealing temperature to the spatial disturbance of the oxygen and shifting of the majority of Ti^{4+} ions by breaking two of the six Ti-O bonds to form new bonds. Moreover, it is stated that rutile nucleation occurs at the interface between two contacting anatase crystals, ultimately resulting in the transformation of smaller anatase grains into large rutile crystals with a growth preference along the nanotube length rather than laterally across the thick oxide layered bottom; this well-explains the calculated grain sizes and unit cell parameters at 600 °C in Table 2.

The expected Ti $L_{3,2}$ and O K-edge shapes when bonded in anatase and rutile are shown in Fig. 4(a) and (b), respectively, as studied by Stoyanov et al. [31]. General line-shapes of these edges when bonded in amorphous TiO_2 and other nanostructured titania can be found in [27–30, 42]. As shown in Fig. 4(a) the Ti $L_{3,2}$ ELNEFS for both anatase and rutile (valency = Ti^{4+}) are split into two distinct peaks, namely L_3 on the lower energy side and L_2 on the high energy loss end, separated by about 5 eV. The L_3 and L_2 white lines are further split into doublets labelled a, b, c, and d, with (a, a') and (b, b') forming the L_3 edge, whereas the L_2 edge comprises of (c,d) doublet. The doublets (a, a') and c originate from the t_{2g} vibrational state, whereas (b, b') and d peaks are ascribed to the e_g energy states. Evident from Fig. 4(c) to (e), when probing the Ti $L_{3,2}$ line-shapes along the nanotube length, different crystal field splitting behavior of the individual L_3 and L_2 white-lines' respective e_g and t_{2g} sub-bands, as indicated by the arrows, are noticed when probing from the bottom (position 1) to the top (position 4) of the tubes. The data presented in Fig. 4 are of nanotubes annealed at 600 °C for 3 h in air at atmospheric pressure. At closer inspection of Ti $L_{3,2}$ line-shape at position 4 of Fig. 4(c) it is found that the t_{2g} band of the L_3 and L_2 edges appear as shoulders (indicated by arrows) on the lower energy side of the e_g band with energy separation of 1.7 eV; this is indicative of rutile according to Fig. 4(a) and in agreement with the XRD data of Fig. 3(c). Towards the bottom of the nanotube, at position 2 of Fig. 4(c), it is noted that the L_3-edge develops an e_g shoulder on the high energy-loss side, which is characteristic of anatase and hints at the coexistence of an anatase/rutile phase. At position 1 the width of the L_3 and L_2 peaks increases due to the negligible difference in intensity of the constituent t_{2g} and e_g sub-bands and as a result the characteristic crystal field splitting of neither anatase nor rutile is observed. This observation is ascribed to the co-existence of anatase and rutile, as well as the presence of amorphous tissue, as observed in TEM micrographs (not shown) in the thick oxide layer that forms the seed layer for nanotube crystal growth. A similar trend is observed in the nanotubes synthesized using type 2 electrolytes in Fig. 4(d). In this case, however, a look at the $L_{3,2}$ signal of position 1 at the nanotube bottom, shows a slight difference to the corresponding shape of Fig. 4(c). A clear splitting of the L_3 and L_2 edges into the t_{2g} and e_g shoulder edges are observed. It is also discriminable from the EELS spectra of position 5, that t_{2g} of the L_2-edge appears as a shoulder on the low energy side of the e_g band which reveal the presence of rutile crystals, whereas the L_3 still possesses the dual shoulder characteristic. Towards the nanotube bottom (position 9), the dual shoulder effect is observed to have initiated also on the L_2-edge resulting in a flat plateau shape, which is an indication of a mixed-phased oxide structure of the TiO_2 nanotube. It can be speculated that the occurrence of the t_{2g} band on the high energy side at the nanotube top (position 1) is indicative of the dominance of anatase phase, whereas towards the nanotube tube bottom it may be ascribed to the rutile dominance. No tangible information on the crystallographic structure could be obtained from the O-K edge shown in Fig. 4(d) due to the poorly-resolved crystal-field splitting. However, it is observed that the O K-edge exhibit changes in line shapes towards the bottom of the nanotube, thus this could be indicative of variations in chemical bond lengths and distortion of the octahedra of the two crystal phases [42]. The findings of the EELS results in Fig. 4(c) to (e) are further substantiated by the electron diffraction results of a single nanotube, shown in Fig. 4 (f, g). The diffraction pattern collected at the nanotube bottom mostly exhibits the amorphous character associated with the thick oxide layer, but with a distinct ring pattern of the rutile (101) plane also clearly visible as the only crystalline feature in this region of the structure. Probing further along the nanotube length shows an increase in diffraction in the middle and anatase domination at the nanotube top, in agreement with the deductions made from the energy loss fine structure of Fig. 4(c), (d) and (e).

The inhomogeneous crystalline nature of the ATNTs synthesized in the three different electrolytes influence the measured optical properties of the structure, in particular the bandgap. Using electron microscopy, this can be achieved by means of valence EELS, or so called VEELS. It must be noted, however, that the use of VEELS in elucidating the optical properties of nanostructures, in the absence of a monochromatic electron source, is very difficult due to the extended tail of the zero loss peak (ZLP). Various methods, both mathematical and experimental, have been developed over the years to remove the tail of the ZLP from low loss EELS spectra, with various success. In this study, the ZLP was removed by collecting a low loss EELS spectrum in vacuum (i.e. in the absence of a specimen) and then mathematically subtracting it from the eventual low loss spectrum, in accordance with the method developed by Potapov et al. [43], which states that the bandgap can be measured at the intersection as shown in Fig. 5. For a single nanotube synthesized in regime 1 type electrolytes and subsequently annealed at 600 °C for 3 h, the VEELS signal was collected at 8 strategic positions along the length of the structure as shown in Fig. 5(a), with the resultant low loss spectrum with the ZLP removed according to [43]

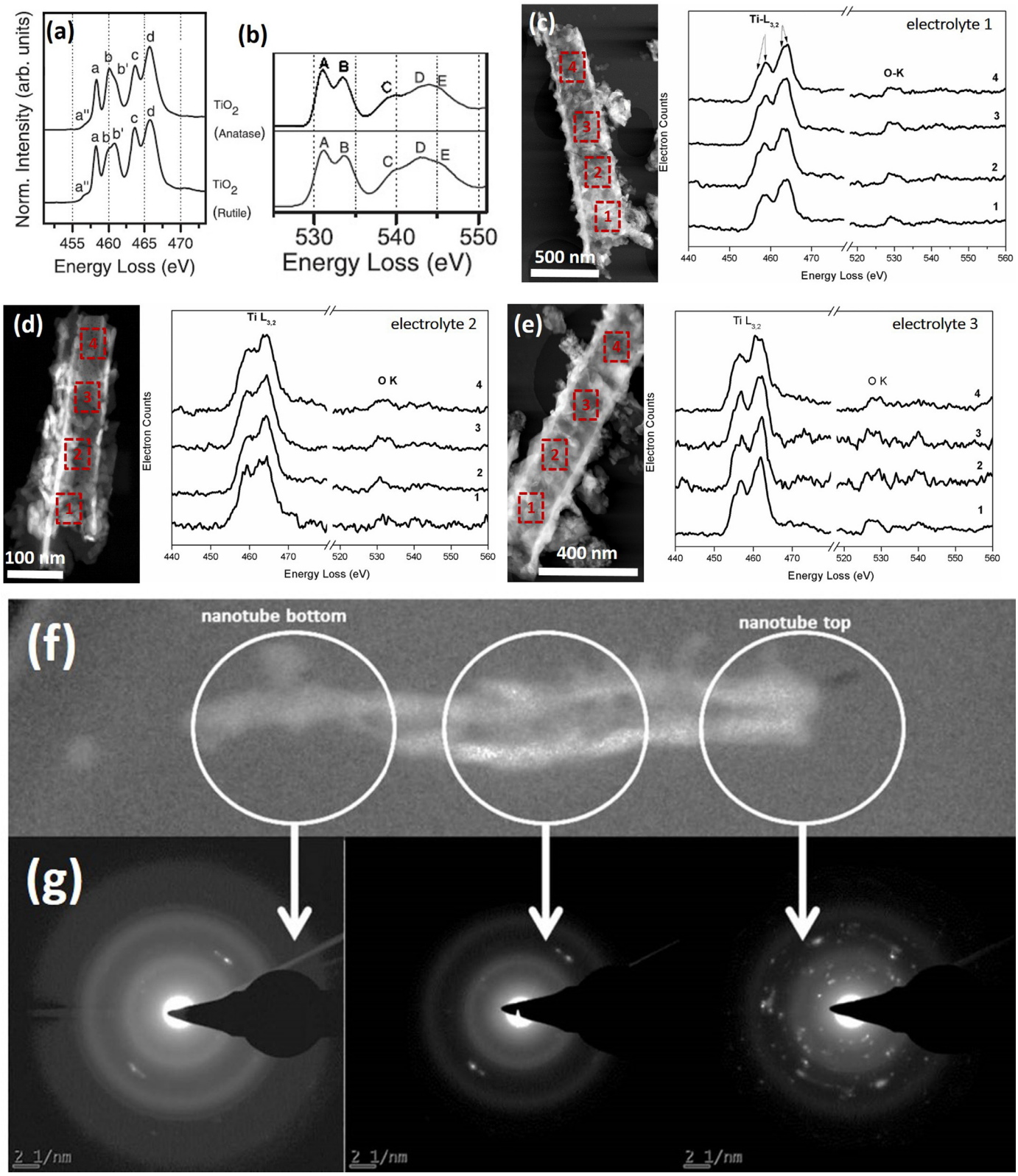

Fig. 4. (a) Ti $L_{3,2}$ and (b) O K edges of different TiO_2 polymorphs [28]; (c) – (e) Ti $L_{3,2}$ and O K edges along the length of individual TiO_2 NTs; (f) STEM-HAADF image with areas selected using a 200 nm selected area aperture for electron diffraction indicated, (g) the corresponding SAED patterns.

shown in Fig. 5(b). From the intersection of these spectra with the vacuum collected ZLP shape, it is found that the bandgap indeed varies along the nanotube length, with a value of 3.44 eV determined for regions near the nanotube bottom and 3.21 eV near the nanotube top. Anatase typically has an optical bandgap of 3.2 eV, whereas pure rutile has a gap of 3.0 eV [44]; as such the values obtained from the VEELS data in Fig. 5(b) can be ascribed to the mixed crystalline phases of anatase and rutile present in a single anodized TiO_2 nanotube as found by the ELNEFS data of Fig. 4.

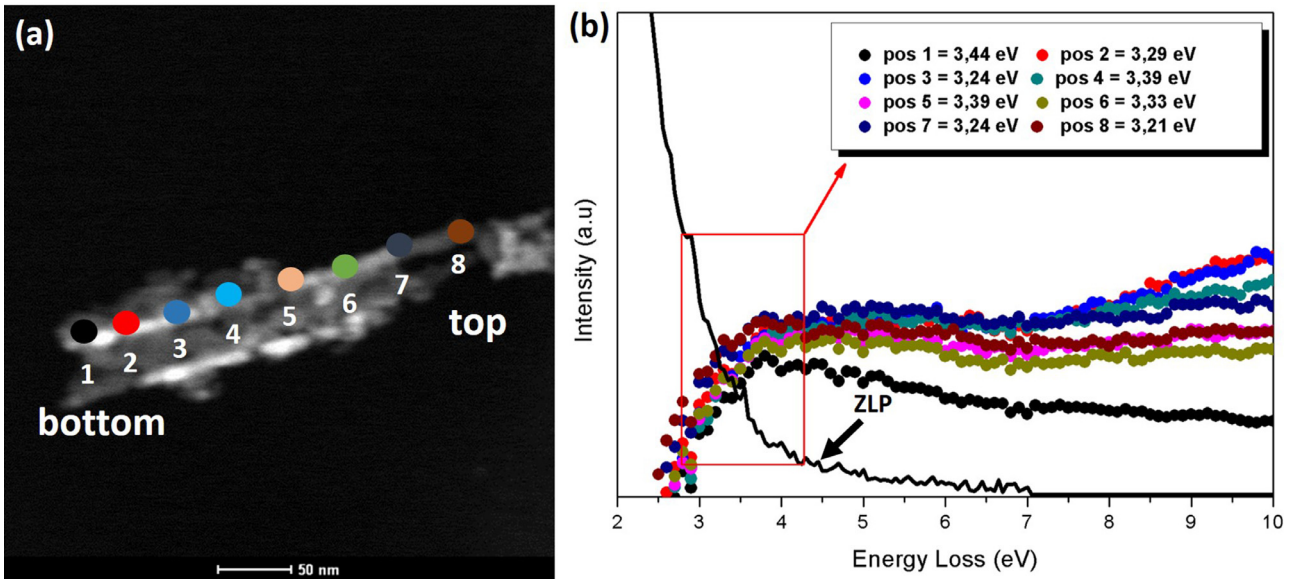

Fig. 5. (a) HAADF micrograph of single nanotube with the positions at which low loss EEL spectra were collected indicated; (b) resultant low loss EELS spectra; (c) ZLP removal from low loss spectrum and determination of bandgap [43].

4. Conclusions

Synthesis of TiO_2 nanotubes in low and highly viscous electrolytes yield morphologies with different wall structures due to the different rates of oxide breakdown. Subsequent annealing at 450 and 600 °C in air at atmospheric pressure crystallizes the nanotubes in anatase and rutile rich crystals respectively. Electron energy loss studies, however, show that individual nanotubes are not exclusively either rutile or anatase, but rather exist in a mixed phase nature along the nanotube length. VEELS studies show that the mixed phase nature of individual nanotubes lead to a variance in the measured bandgap along the length of the nanotube.

Acknowledgements

The authors would like to thank Prof Tommi White of the Electron Microscopy Core Facility at University of Missouri-Columbia for allowing access to the Tecnai F30 HRTEM and collection of the microscopy data presented in the manuscript.

This work was supported by the National Research Foundation, South Africa (grant number: TTK170405225919; UID: 113277).

Conflict of Interest

none

References

[1] X. Feng, K. Shankar, O.K. Varghese, M. Paulose, T.J. Latempa, C.A. Grimes, Vertically aligned single crystal TiO_2 nanowire arrays grown directly on transparent conducting oxide coated Glass: synthesis details and applications, Nano Lett. 8 (2008) 3781–3786, https://doi.org/10.1021/nl802096a.

[2] R. Tenne, C.N.R. Rao, Inorganic nanotubes, Philos. Trans. R. Soc. A 362 (2004) 2099–2125, https://doi.org/10.1098/rsta.2004.1431.

[3] A.J. Frank, N. Kopidakis, J. Van De Lagemaat, Electrons in nanostructured TiO_2 solar cells: transport, recombination and photovoltaic properties, Coord. Chem. Rev. 248 (2004) 1165–1179, https://doi.org/10.1016/j.ccr.2004.03.015.

[4] D. Gong, C.A. Grimes, O.K. Varghese, W. Hu, R.S. Singh, Z. Chen, E.C. Dickey, Titanium oxide nanotube arrays prepared by anodic oxidation, J. Mater. Res. 16 (2001) 3331–3334, https://doi.org/10.1557/JMR.2001.0457.

[5] G.K. Mor, O.K. Varghese, M. Paulose, K. Shankar, C.A. Grimes, A review on highly ordered, vertically oriented TiO_2 nanotube arrays: fabrication, material properties, and solar energy applications, Sol. Energy Mater. Solar Cells 90 (2006) 2011–2075, https://doi.org/10.1016/j.solmat.2006.04.007.

[6] M. Paulose, K. Shankar, O.K. Varghese, G.K. Mor, C.A. Grimes, Application of highly-ordered TiO_2 nanotube arrays in heterojunction dye-sensitized solar cells, J. Phys. D Appl. Phys. 39 (2006) 2498–2503, https://doi.org/10.1088/0022-3727/39/12/005.

[7] H. Park, W.-R. Kim, H.-T. Jeong, J.-J. Lee, H.-G. Kim, W.-Y. Choi, Fabrication of dye-sensitized solar cells by transplanting highly ordered TiO_2 nanotube arrays, Sol. Energy Mater. Sol. Cells 95 (2011) 184–189, https://doi.org/10.1016/j.solmat.2010.02.017.

[8] K. Shankar, G.K. Mor, H.E. Prakasam, S. Yoriya, M. Paulose, O.K. Varghese, C.A. Grimes, Highly-ordered TiO2 nanotube arrays up to 220μm in length: use in water photoelectrolysis and dye-sensitized solar cells, Nanotechnology 18 (2007), https://doi.org/10.1088/0957-4484/18/6/065707 065707- 065711.

[9] D.J. Yang, H. Park, S.J. Cho, H.G. Kim, W.Y. Choi, TiO_2-nanotube-based dye-sensitized solar cells fabricated by an efficient anodic oxidation for high surface area, J. Phys. Chem. Solids 69 (2008) 1272–1275, https://doi.org/10.1016/j.jpcs.2007.10.107.

[10] H.E. Prakasam, K. Shankar, M. Paulose, O.K. Varghese, C.A. Grimes, A new benchmark for TiO_2 nanotube array growth by anodization, J. Phys. Chem. C 111 (2007) 7235–7241, https://doi.org/10.1021/jp070273h.

[11] J.M. Macak, H. Tsuchiya, L. Taveira, S. Aldabergerova, P. Schmuki, Smooth anodic TiO nanotubes, Angew. Chem. 117 (2005) 7629–7632, https://doi.org/10.1002/anie.200502781.

[12] S. Sreekantan, R. Hazan, Z. Lockman, Photoactivity of anatase–rutile TiO_2 nanotubes formed by anodization method, Thin Solid Films 518 (2009) 16–21, https://doi.org/10.1016/j.tsf.2009.06.002.

[13] F.R. Cummings, T.F.G. Muller, G.F. Malgas, C.J. Arendse, Investigation of the growth and local stoichiometric point group symmetry of titania nanotubes during potentiostatic anodization of titanium in phosphate electrolytes, J. Phys. Chem. Solids 85 (2015) 278–286, https://doi.org/10.1016/j.jpcs.2015.06.009.

[14] R.D. Leapman, L.A. Grunes, P.L. Fejes, Study of the L_{23} edges in the 3d transition metals and their oxides by electron-energy-loss spectroscopy with comparisons to theory, Phys. Rev. B 26 (1982) 614–635, https://doi.org/10.1103/PhysRevB.26.614.

[15] D.H. Pearson, C.C. Ahn, B. Fultz, White lines and d-electron occupancies for the 3d and 4d transition metals, Phys. Rev. B 47 (1993) 8471–8478, https://doi.org/10.1103/PhysRevB.47.8471.

[16] H. Tan, J. Verbeeck, A. Abakumov, G. Van Tendeloo, Oxidation state and chemical shift investigation in transition metal oxides by EELS, Ultramicroscopy 116 (2012) 24–33, https://doi.org/10.1016/j.ultramic.2012.03.002.

[17] M. Stöger-Pollach, P. Schattschneider, The influence of relativistic energy losses on bandgap determination using valence EELS, Ultramicroscopy 107 (2007) 1178–1185, https://doi.org/10.1016/j.ultramic.2007.01.015.

[18] T. Kiguchi, Wakiya N, K. Shinozaki, T. Konno, Valence-EELS analysis of local electronic and optical properties of PMN–PT epitaxial film, Mater. Sci. Eng. B 161 (2009) 160–165, https://doi.org/10.1016/j.mseb.2009.01.015.

[19] K. Kimoto, T. Asaka, T. Nagai, M. Saito, Y. Matsui, K. Ishizuka, Element-selective imaging of atomic columns in a crystal using STEM and EELS, Nature 405 (2007) 702–704, https://doi.org/10.1038/nature06352.

[20] G. Nicotra, A. Politano, A.M. Mio, I. Deretzis, J. Hu, Z.Q. Mao, J. Wei, A. La Magna, C. Spinella, Absorption edges of black phosphorus: a comparative analysis, Phys. Status Solidi B 253 (2016) 2509–2514, https://doi.org/10.1002/pssb.201600437.

[21] G. Nicotra, E. Van Veen, I. Deretzis, L. Wang, J. Hu, Z. Mao, et al., Anisotropic ultraviolet-plasmon dispersion in black phosphorus, Nanoscale 10 (2018) 21918–21927, https://doi.org/10.1039/c8nr05502e.

[22] A. Politano, G. Chiarello, C. Spinella, Plasmon spectroscopy of graphene and other

two-dimensional materials with transmission electron microscopy, Mater. Sci. Semicond. Process. 65 (2017) 88–99, https://doi.org/10.1016/j.mssp.2016.05.00.
[23] G. Nicotra, A.M. Mio, A. Cupolillo, J. Hu, STEM and EELS investigation on black phosphorus at atomic resolution, Microsc. Microanal. 21 (2015) 427–428, https://doi.org/10.1017/S1431927615002937.
[24] D.M. Kepaptsoglou, D. Gilks, L. Lari, Q.M. Ramasse, P. Galindo, M. Weinert, et al., STEM and EELS study of the graphene/Bi_2Se_3 interface, Microsc. Microanal. 21 (2015) 1151–1152, https://doi.org/10.1017/S1431927615006546.
[25] M.K. Kinyanjui, C. Kramberger, T. Pichler, J.C. Meyer, P. Wachsmuth, G. Benner, U. Kaiser, Direct probe of linearly dispersing 2D interband plasmons in a free-standing graphene monolayer, Europhys. Lett. 97 (2012) 57005, https://doi.org/10.1209/0295-5075/97/57005.
[26] S.J. Pennycook, M. Varela, New views of materials through aberration-corrected scanning transmission electron microscopy, J. Electron. Microsc. 60 (2011) S213–S223, https://doi.org/10.1093/jmicro/dfr030.
[27] L.A. Grunes, Study of the k edges of 3d transition metals in pure and oxide form by x-ray-absorption spectroscopy, Phys. Rev. B 27 (1983) 2111–2131, https://doi.org/10.1103/PhysRevB.27.2111.
[28] R. Brydson, J.M. Thomas, Electron energy-loss spectroscopy (EELS) and the electronic structure of titanium dioxide, Solid State Commun. 64 (1987) 609–612, https://doi.org/10.1016/0038-1098(87)90792-7.
[29] R. Brydson, H. Sauer, W. Engel, J.M. Thomas, E. Zeitler, N. Kosugi, H. Kuroda, Electron energy loss and x-ray absorption spectroscopy of rutile and anatase: a test of structural sensitivity, J. Phys. Condens. Matter l (1989) 797–812, https://doi.org/10.1088/0953-8984/1/4/012.
[30] R. Brydson, H. Sauer, W. Engel, F. Hofer, Electron energy-loss near-edge structures at the oxygen K edges of titanium (IV) oxygen compounds, J. Phys. Condens. Matter 4 (1992) 3429–3437, https://doi.org/10.1088/0953-8984/4/13/007.
[31] E. Stoyanov, F. Langenhorst, G. Steinle-Neumann, The effect of valence state and site geometry on Ti $L_{3,2}$ and O K electron energy-loss spectra of Ti_xO_y phases, Am. Mineral. 92 (2007) 577–586, https://doi.org/10.2138/am.2007.2344.
[32] G. Bertoni, E. Beyers, J. Verbeeck, M. Mertens, P. Cool, E.F. Vansant, G. Van Tendeloo, Quantification of crystalline and amorphous content in porous samples from electron energy loss spectroscopy, Ultramicroscopy 106 (2006) 630–635, https://doi.org/10.1016/j.ultramic.2006.03.006.
[33] F.R. Cummings, L.J. Le Roux, M.K. Mathe, D. Knoesen, Structure induced optical properties of anodized TiO_2 nanotubes, Mater. Chem. Phys. 124 (2010) 234–242, https://doi.org/10.1016/j.matchemphys.2010.06.024.
[34] T. Akita, M. Okumura, K. Tanaka, K. Ohkuma, M. Kohyama, T. Koyanagi, M. Date, S. Tsubota, M. Haruta, Transmission electron microscopy observation of the structure of TiO_2 nanotube and Au/TiO_2 nanotube catalyst, Surf. Interface Anal. 37 (2005) 265–269, https://doi.org/10.1002/sia.1979.
[35] D. Regonini, G. Chen, C. Leach, F.J. Clemens, Comparison of photoelectrochemical properties of TiO_2 nanotubes and sol-gel, Electrochim. Acta 213 (2016) 31–36, https://doi.org/10.1016/j.electacta.2016.07.097.
[36] J.M. Macak, H. Tsuchiya, A. Ghicov, K. Yasuda, R. Hahn, S. Bauer, P. Schmuki, TiO nanotubes, Self-organized electrochemical formation, properties and applications, Curr. Opin. Solid State Mater. Sci. 11 (2007) 3–18, https://doi.org/10.1016/j.cossms.2007.08.004.
[37] P. Roy, S. Berger, P. Schmuki, TiO nanotubes: synthesis and applications, Angew. Chem. Int. Ed. 50 (2011) 2904–2939, https://doi.org/10.1002/anie.201001374.
[38] V.C. Anitha, A.N. Banerjee, S.W. Joo, B.K. Min, Barrier-oxide layer engineering of TiO_2 nanotube arrays to get single- and multi-stage Y-branched nanotubes: effect of voltage ramping and electrolyte conductivity, Mater. Sci. Eng. B 195 (2015) 1–11, https://doi.org/10.1016/j.mseb.2015.01.005.
[39] V.D. Mote, Y. Purushotham, B.N. Dole, Williamson-Hall analysis in estimation of lattice strain in nanometer-sized ZnO particles, J. Theor. Appl. Phys. 6 (2012) 6, https://doi.org/10.1186/2251-7235-6-6.
[40] D. Regonini, A. Jaroenworaluck, R. Stevens, C.R. Bowen, Effect of heat treatment on the properties and structure of TiO_2 nanotubes: phase composition and chemical composition, Surf. Interface Anal. 42 (2010) 139–144, https://doi.org/10.1002/sia.3183.
[41] O.K. Varghese, D. Gong, M. Paulose, E.C. Dickey, C.A. Grimes, Crystallization and high-temperature structural stability of titanium oxide nanotube arrays, J. Mater. Res. 18 (2003) 156–165, https://doi.org/10.1557/JMR.2003.0022.
[42] S.O. Kucheyev, T. Van Buuren, T.F. Satcher Jr., T.M. Willey, R.W. Meulenberg, T.E. Felter, et al., Electronic structure of titania aerogels from soft x-ray absorption spectroscopy, Phys. Rev. B. 69 (2004) 245102, , https://doi.org/10.1103/PhysRevB.69.245102.
[43] P.L. Potapov, H.-J. Engelmann, E. Zschech, M. Stoger-Pollach, Measuring the dielectric constant of materials from valence EELS, Micron 40 (2009) 262–268, https://doi.org/10.1016/j.micron.2008.07.006.
[44] T. Luttrell, S. Halpegamage, J. Tao, A. Kramer, E. Sutter, M. Batzill, Why is anatase a better photocatalyst than rutile? - Model studies on epitaxial TiO_2 films, Sci. Rep. 4 (2014) 4043, https://doi.org/10.1038/srep04043.